

Temperature dependence of magnetic excitations in the topological insulator CoTiO₃

Srimal Rathnayaka¹,¹ Luke Daemen,² John A. Schneeloch,¹ Yongqiang Cheng,² and Despina Louca^{1,*}

¹*Department of Physics, University of Virginia, Charlottesville, Virginia 22904, USA*

²*Neutron Scattering Division, Oak Ridge National Laboratory, Oak Ridge, Tennessee 37831, USA*

 (Received 10 October 2023; revised 27 March 2024; accepted 29 March 2024; published 20 May 2024)

Magnetic excitons and spin-orbit transitions are investigated in the pseudospin- $\frac{1}{2}$ CoTiO₃ Dirac magnon system using inelastic neutron scattering. The magnon density of states consists of two magnon peaks with a gapless Dirac node nestled between them. Above 38 K, the Néel temperature (T_N), the magnon modes are renormalized to lower energies. Magnetic excitations attributed to spin-orbit exciton multiplet transitions follow the same temperature dependence as the magnons, with the intensity dissipating quickly above T_N . On the other hand, energy level transitions arising from the crystal field and spin-orbit coupling (with an estimated $\lambda \approx 14$ meV) are gradually thermally populated, continuing through T_N and reaching a maximum at ~ 100 K. The excitations significantly broaden but persist through room temperature.

DOI: [10.1103/PhysRevB.109.174432](https://doi.org/10.1103/PhysRevB.109.174432)

I. INTRODUCTION

The discovery of Dirac fermions with their signature linear dispersion relations in honeycomb lattices such as graphene has led to an explosion of exciting new phenomena in condensed-matter physics [1–3]. Various bosonic analogs have been proposed as well; these are charge-neutral systems with no valence and conduction bands, and with linear band crossing points occurring at finite energies. An example is the Dirac magnons that emerge at the intersection of acoustic and optical spin waves in honeycomb- and kagome-type lattices [4]. The topologically nontrivial band structures in bosonic systems are predicted to give rise to behaviors such as the spin Nernst effect and the thermal Hall effect [5,6]. Included in this class are halides CrX₃ ($X = \text{Cl, Br, I}$) [7] and ilmenites ATiO₃ ($A = \text{Co, Ni, and Mn}$) [8–10] consisting of weakly bound van der Waals (vdW) layers, serving as the magnetic analogs of graphene. A compelling candidate for the manifestation of topological spin excitations is CoTiO₃, characterized by a quasi-two-dimensional honeycomb lattice [8,11]. Beyond its Dirac magnon characteristics, CoTiO₃ is known for its unquenched orbital angular momentum, L , giving rise to spin-orbit coupling (SOC), and is host to magnetic excitons [10]. The roles of excitons and SOC have been discussed in a number of systems with a Co²⁺ 3d⁷ electronic configuration [12] such as in KCoF₃, CoO, (La/Sr)₂CoO₄, and GeCo₂O₄, to name a few [13–18].

Following conventional band theory, CoTiO₃ has an odd number of electrons in the valence band and should be metallic. However, CoTiO₃ is a strong insulator, a consequence of strong correlations. The unquenched $L_{\text{eff}} \approx 1$ is supported by the absence of lattice distortions, orbital ordering, or Jahn-Teller coupling, and the superexchange interactions are presumed to be weak [19]. Co²⁺ is also host to a pseudospin- $\frac{1}{2}$ magnetism. It is this spin that gives CoTiO₃ its magnetic

characteristics. Co²⁺ in the octahedral 3d⁷ configuration consists of one spin in the t_{2g} orbital and two spins in the e_g orbitals. Co²⁺ spins couple antiferromagnetically (AFM) across the vdW layers. In ilmenites, it has been proposed by Goodenough and Stickler [10] that exciton transfer may occur via the superexchange paths. On the other hand, the Co²⁺ spins couple ferromagnetically in-plane through both direct exchange between transition metal ions, or mediated through oxygen. CoTiO₃ is a system where crystal field and spin-orbit excitations are strongly coupled to the magnetism.

CoTiO₃ crystallizes in the trigonal $R\bar{3}$ space group. The oxygen atoms form trigonally distorted octahedra around both Co and Ti as depicted in Fig. 1(a). The Co atoms reside in honeycomb layers, with a $\frac{1}{3}$ shift between adjacent layers as shown in Fig. 1(b). The AFM stacking of the layers along the c axis exhibits a Néel transition (T_N) at 38 K [20]. Recent neutron scattering experiments explored the presence of Dirac magnons and magnetic excitations and suggested the existence of Dirac nodal lines resulting from a bond-dependent exchange coupling described by an XXZ spin model [8,11]. These experiments also indicated the presence of a Dirac gap [20] and bond-dependent coupling [8].

Starting from the unquenched $L_{\text{eff}} = 1$ and $S = \frac{3}{2}$, the total angular momentum J -manifold splits under $\lambda(LS)$ coupling into $\frac{1}{2}$, $\frac{3}{2}$, and $\frac{5}{2}$ levels. These spin-orbit levels are separated by $\frac{3}{2}\lambda$ and $\frac{5}{2}\lambda$. Magnetic exchange interactions split these levels further into nondegenerate $J_z = \pm\frac{1}{2}$, $J_z = \pm\frac{1}{2}$ and $\pm\frac{3}{2}$, and $J_z = \pm\frac{1}{2}$, $\pm\frac{3}{2}$, and $\pm\frac{5}{2}$ [10]. The ground state is $J_z = \pm\frac{1}{2}$, a Kramer's doublet, that makes the Co²⁺ ion the host of a pseudospin- $\frac{1}{2}$ magnetism. A schematic of the energy states is shown in Fig. 1(c) [10]. The octahedral environment sets up the crystal field splitting that leads to the pseudospin- $\frac{1}{2}$. The edge-sharing octahedra are grounds for bond-dependent exchange interactions [21]. The family of d^7 cobaltates with pseudospin- $\frac{1}{2}$ ground states, such as CoNb₂O₆, Ba₃CoSb₂O₉, Ba₈CoNb₆O₂₄, GeCo₂O₄, and

*Corresponding author: louca@virginia.edu

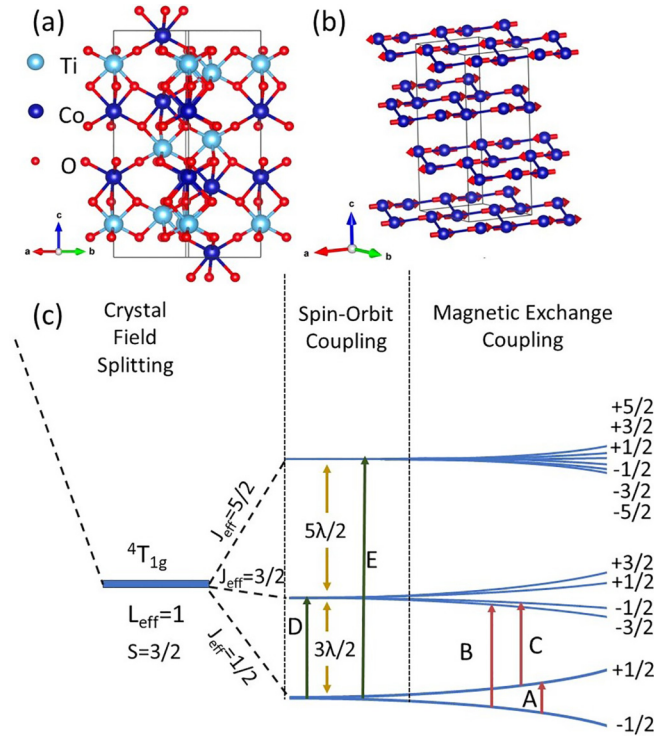


FIG. 1. (a) The unit cell of CoTiO₃ in the hexagonal representation with $R\bar{3}$ symmetry. (b) The antiferromagnetic honeycomb lattice with the spins aligned in the same direction in-plane and in opposite directions across planes. All the Co²⁺ ions in the honeycomb layer are not in the same plane because of distortions in the structure. (c) Schematic diagram of the energy level splitting of T_{1g} .

NaCaCo₂F₇, has garnered significant attention due to their quantum magnetism and topological phases [18,22–26].

Materials with these characteristics are promising in spin-related optical applications [15,27–29]. Excitons couple to the spin and orbital degrees of freedom, forming an exotic quasiparticle, the spin-orbit exciton (SOE). The SOEs in CoTiO₃ are dressed with magnons. Similar observations have been made in Sr₂IrO₄ [30], KCoF₃ [14], and CoO [16]. Notably, the presence of strong SOC in transition metals enables the formation of SOEs, with d^7 Co²⁺ being an exemplary system. In this work, we focus on the temperature dependence of the excitations. Low-energy magnons show strong damping on warming, but the inelastic intensity persists above T_N . Multiplet transitions are simultaneously observed. These are suppressed above T_N , while transitions between spin-orbit levels continue to be observed. Evidence for these transitions persists up to room temperature.

II. EXPERIMENTAL DETAILS

CoTiO₃ powder was prepared using the solid-state reaction method. Co₃O₄ and TiO₂ powders were thoroughly mixed in a 1:3 molar ratio and subsequently reacted at 1200 °C in a tube furnace under an argon gas environment for 48 h. Neutron scattering measurements were carried out using the VISION time-of-flight (TOF) spectrometer at the Spallation Neutron Source at Oak Ridge National Laboratory. A 10-g powder sample was utilized for the measurement, in which

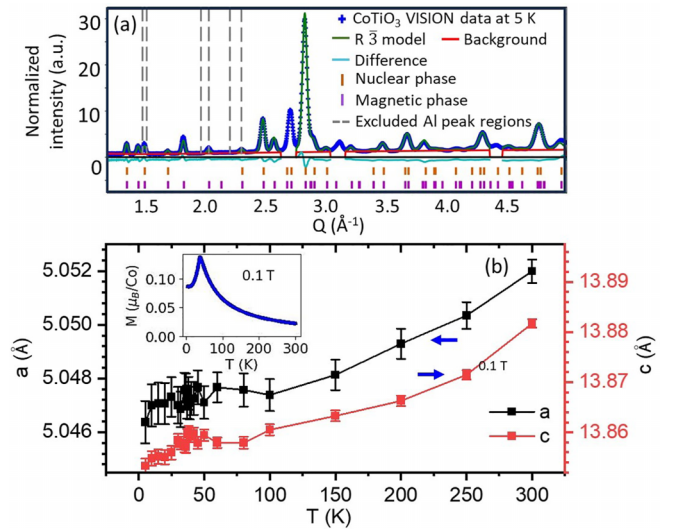


FIG. 2. (a) The diffraction pattern (blue line) is compared to the fitting (green line) at 5 K. Also shown is the difference between the two (cyan line). The red tick marks indicate nuclear peaks and the green tick marks indicate magnetic peaks. The dotted lines represent aluminum peaks from the sample holder, which were excluded from the fitting. (b) The temperature dependence of the lattice parameters a and c was obtained from the elastic data refinement. The inset is the magnetic susceptibility as a function of temperature at $H = 0.1$ T.

elastic and inelastic data were acquired simultaneously in the temperature range of 5 to 300 K. The final neutron energy was fixed at 3.5 meV. Data in two narrow paths in energy and momentum (Q) space were collected, labeled as the high- Q and low- Q paths, corresponding to 45° and 135°, respectively. The corresponding Q range is 1.5 to 30 Å⁻¹. The refinement of the elastic data confirmed the presence of a single CoTiO₃ phase in the system at 5 K. The magnon dispersions were simulated using the MATLAB package SPINW [31].

III. RESULTS AND DISCUSSION

Shown in Fig. 2(a) is the elastic neutron scattering intensity at 5 K. The diffraction data include both nuclear and magnetic Bragg peaks. As the temperature rises, the intensity of the magnetic peaks weakens, ultimately disappearing at $T_N = 38$ K. This temperature marks the system's transition from the AFM to the paramagnetic phase. The Rietveld refinement of the diffraction data confirmed the presence of the R $\bar{3}$ phase at all temperatures. Furthermore, the refinement provided the lattice parameters a and c shown in Fig. 2(b), largely showing conventional thermal expansion behavior. However, an anomaly is observed near T_N . This effect has been attributed to magnetoelastic coupling [32,33]. The kink seen in both parameters marks a different behavior above and below T_N . Below T_N , both a and c exhibit a more linear expansion, while above T_N this linearity diminishes. Below T_N , the change in lattice parameters is approximately 0.002 Å for a and 0.01 Å for c . These trends show the anisotropy of the structural changes below T_N , attributed to the stronger in-plane than out-of-plane magnetic coupling [11]. A similar behavior is also observed in isostructural and magnetically similar NiTiO₃ and MnTiO₃ [34,35].

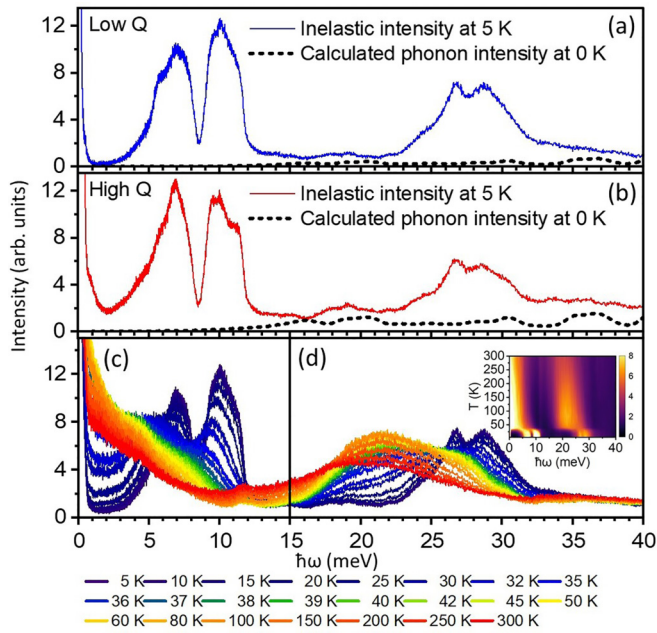


FIG. 3. The magnetic density of states (DOS) obtained from the VISION instrument along the (a) low- Q path and (b) the high- Q path at 5 K is plotted as a function of energy transfer ($\hbar\omega$) in blue. The instrument and empty can backgrounds were subtracted from the data. The phonon DOS was calculated at 0 K (black dotted line), but it was not subtracted from the data due to its negligible contribution. (c) The magnetic DOS is plotted as a function of temperature ranging from 5 to 300 K. The intensity within $0 < \hbar\omega \leq 15$ meV is purely magnon. (d) The higher-energy region from 15 to 40 meV corresponds to multiplet transitions of the magnetic excitons and SO split levels. The inset is an intensity map of the low- Q inelastic data, which corresponds to the data presented in panels (c) and (d).

The magnetic structure can be described by a propagation wave vector $\mathbf{k} = (003/2)$, as shown in Fig. 1(b). The magnetic moment M was refined along with the structural parameters. The spins align with the easy plane and have magnitude $M = 3.23\mu_B$ at 5 K, consistent with a previous report [8]. Shown in the inset of Fig. 2(b) is the magnetic susceptibility $\chi(T)$. The susceptibility conforms to the typical behavior exhibited by AFM systems, namely, a sharp upturn on cooling followed by a drop in the AFM phase. The apex of this curve corresponds to the Néel point, which has been determined to be 38 K in this system.

The magnon density of states obtained from the dynamic susceptibility of the neutron inelastic powder measurement is plotted as a function of energy in Figs. 3(a) and 3(b) for low- Q and high- Q paths respectively. The dynamic structure function was integrated along the low- Q and high- Q trajectories. The data are compared to the 0 K phonon calculation (black dotted line). The phonon intensity is much weaker compared to the magnon features observed in the 5 K low- Q inelastic data, indicating that the contribution from phonons is negligible in the momentum transfer range sampled by the VISION instrument as shown in Fig. 3(a). By comparison, the phonon signals are stronger along the high- Q path in Fig. 3(b), as expected from the general Q^2 dependence of phonon intensity in neutron scattering. Thus, in this energy and momentum

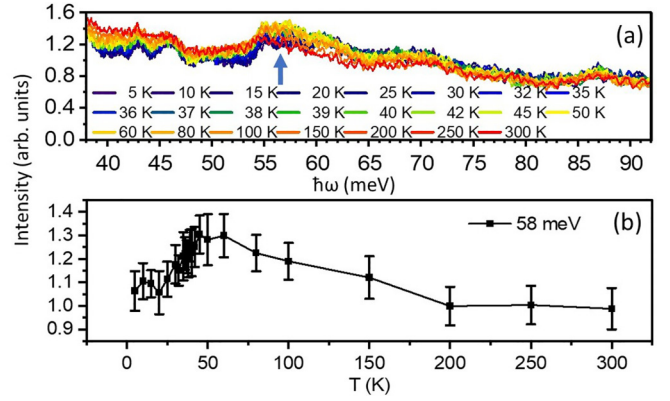


FIG. 4. (a) The temperature dependence of the inelastic intensity from 35 to 95 meV. The blue arrow points to the 58-meV peak. (b) The change of intensity at 58 meV as a function of temperature.

range, the contribution from phonons can be neglected. Shown in Figs. 3(c) and 3(d) are the inelastic spectra plotted for a variety of temperatures. The first two peaks around 5 and 10 meV are from the magnon dispersion arising from excitations of the $J_z = \pm 1/2$ doublet [19], the lowest-energy doublet shown in Fig. 1(c). The crossing point is where the Dirac node appears. It appears to be gapless, though the intensity between the peaks never quite reaches zero even at the lowest measured temperature. Meanwhile, in the 15–40 meV energy range, several additional peaks are observed, with their own clear temperature dependence. The double-peak feature in the 23 to 33 meV range arises due to magnetic transitions in the excited multiplet and exhibits the same temperature dependence as the magnon peaks. These higher-energy peaks are attributed to SOEs. On the other hand, the intensity within the 15–23 meV range exhibits a different temperature dependence. Specifically, the intensity grows as a function of temperature and broadens on approaching 300 K. These excitations arise from populating crystal-field-split spin-orbit levels. Disorder in the lattice with increasing thermal fluctuations can broaden the peaks.

Shown in Fig. 4(a) is the temperature dependence of inelastic intensity up to 100 meV. The peak appearing at approximately 58 to 61 meV corresponds to the transition E indicated in Fig. 1(c). This mode has been reported in Ref. [11], but its temperature dependence was never investigated. Up until T_N , the intensity of this peak shows an increasing behavior. Beyond T_N , the intensity gradually decreases. These spectra show a temperature dependence similar to that of the modes observed in the 15–23 meV range, which are attributed to SOEs.

In Fig. 5(a), the powder-average simulation of the spin-wave dispersion is plotted using a Heisenberg Hamiltonian with six interactions. Specifically, we consider three intraplane exchange interactions (J_1 , J_3 , and J_5) and three interplane exchange interactions (J_2 , J_4 , and J_6). The bonds of these exchange interactions are shown in the inset of Fig. 5(d). Table I lists the J values for three models, with the on-diagonal components (J_x , $J_x = J_y$, and J_z) listed. Models 1 and 2 are from analysis of single-crystal neutron data in the literature (from Refs. [11] and [8], respectively) while Model

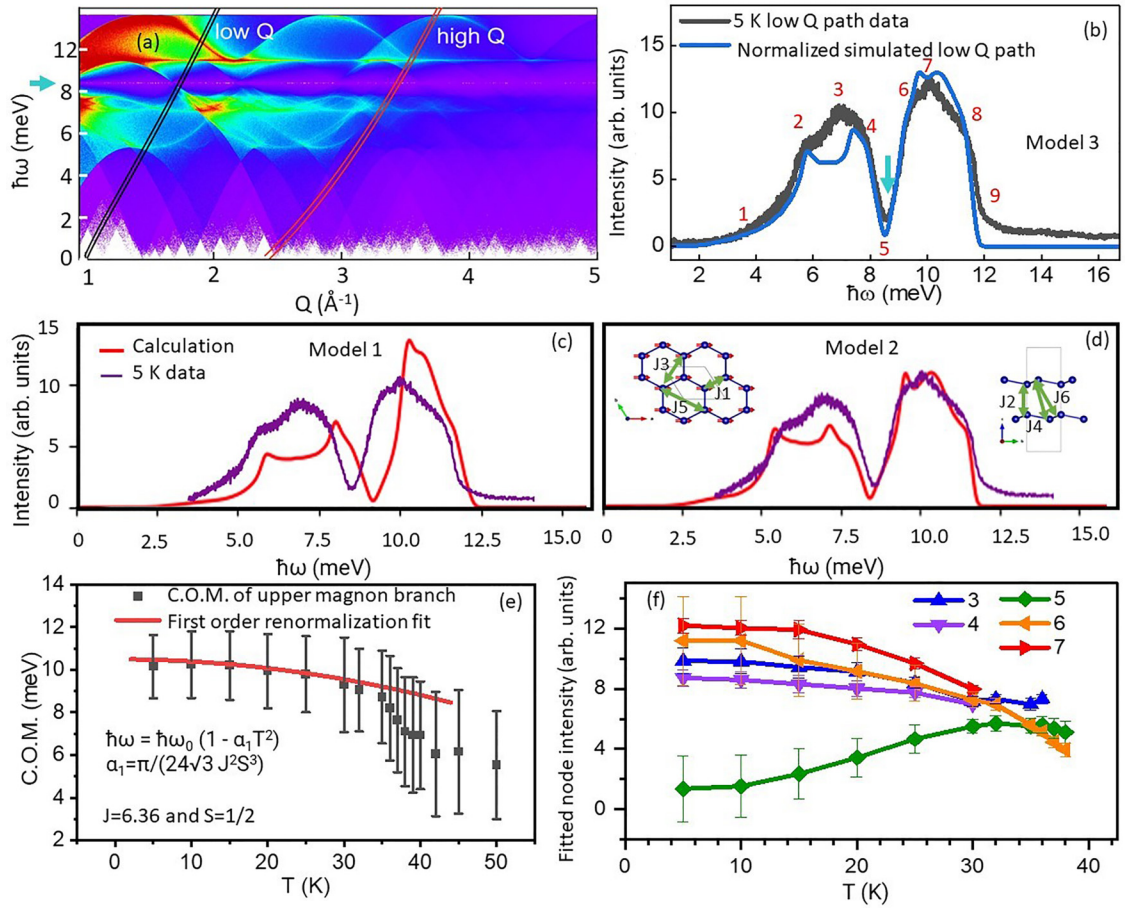


FIG. 5. (a) A spin-wave simulation of the powder-averaged $S_{\perp}(Q, \omega)$ at 0 K. The trajectories represent the low- Q and high- Q paths of the VISION instrument. The blue arrow indicates the Dirac energy level. (b) Comparison between the low- Q inelastic scattering intensity and the calculated $S_{\perp}(Q, \omega)$ at 5 K. The blue arrows correspond to the Dirac energy level. Numbers indicate the node points, special features of the intensity which generally correspond to local maxima, minima, or saddle points of the magnon dispersion. (c) and (d) Comparison of the 5 K low- Q inelastic scattering data (purple) and the calculated $S_{\perp}(Q, \omega)$ for 0 K (red) Models 1 and 2, corresponding, respectively, to those reported in Refs. [11] and [8]. Shown in the inset to panel (d) are the bonds corresponding to the different exchange interactions listed in Table I, indicated as arrows between Co atoms. The left inset shows intralayer interactions as viewed along c , and the right inset shows interlayer interactions as viewed along a . (e) A plot of the center of mass (C.O.M.) of the upper magnon branch as a function of T and the expected first-order renormalization fit for a honeycomb ferromagnet with nearest-neighbor interactions [4]. (f) Intensity vs temperature of the positions numbered in panel (b).

3 consists of the same values as model 2, except with the J_z component set to 0 for J_2 to J_5 , which was observed to result in a better agreement with data in terms of the position of the Dirac node. While Models 1 and 2 were obtained with the

TABLE I. The exchange interactions of three models using the XXZ Hamiltonian.

J	Model 1 Ref. [11]	Model 2 Ref. [8]	Model 3 Present paper
J_1	(-4.41, -4.41, 0)	(-6.36, -6.36, 1.97)	(-6.36, -6.36, 1.97)
J_2	(0, 0, 0)	(-0.33, -0.33, 0.30)	(-0.33, -0.33, 0)
J_3	(0, 0, 0)	(0.78, 0.78, 0.15)	(0.78, 0.78, 0)
J_4	(0.57, 0.57, 0.57)	(0.11, 0.11, 0.32)	(0.11, 0.11, 0)
J_5	(0, 0, 0)	(-0.39, -0.39, 0.20)	(-0.39, -0.39, 0)
J_6	(0.57, 0.57, 0.57)	(0.79, 0.79, 0.68)	(0.79, 0.79, 0)

advantage of using single-crystal neutron scattering, which retains directional information, Model 3 was obtained with the benefit of the exceptional energy resolution of VISION, which allows the Dirac point position to be better located. To simulate the magnon DOS, the integrated intensities along the high- Q and low- Q trajectories were computed and the results for the low- Q trajectory are shown in Fig. 5(b) for Model 3, and more generally as the powder-averaged magnon intensity map in Fig. 5(a). Also shown in Fig. 5(b) is the inelastic intensity at 5 K along the low- Q path. The calculations accounted for the energy resolution of the instrument and set the Q resolution to 0.2 \AA^{-1} . Using the J 's listed in Table I under Model 3, the simulation captures most of the features evident in the data, especially as compared with Models 1 [Fig. 5(c)] and 2 [Fig. 5(d)]. In particular, we note that the width of the Dirac node in the Model 3 calculated intensity is very close to that of the data itself, verifying the gapless nature of the Dirac dispersion in CoTiO_3 . A plot of the intensity of the center

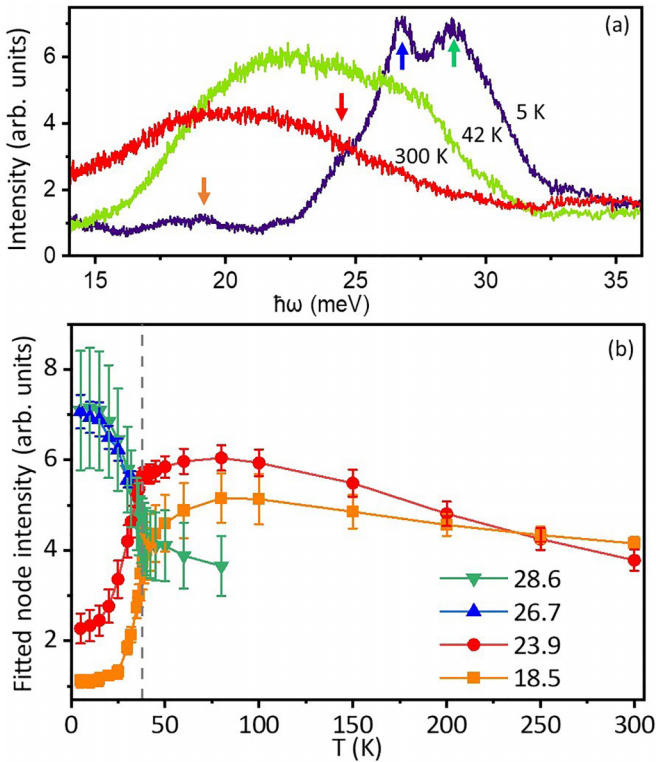


FIG. 6. (a) The inelastic intensity at 5, 42, and 300 K is plotted along the low- Q trajectory. The arrows correspond to the selected nodes. (b) The temperature dependencies at the select nodal points are shown in panel (a). The intensities of the given points were calculated using a fitted function to the data (fitted node intensity).

of mass (C.O.M.) of the higher-energy magnon branch as a function of temperature is shown in Fig. 5(e). The higher-energy branch softens more rapidly than can be accounted for by the first-order magnon-magnon renormalization for a honeycomb ferromagnet, shown as the red curve. Thus, the magnons in CoTiO_3 exhibit significant broadening in energy and shift to lower energies, as shown by the 3-meV decrease in the C.O.M. position from 5 to 50 K.

Shown in Fig. 5(f) is the intensity vs temperature of certain features of the magnon peak intensity and the numbers correspond to Fig. 5(b). The numbers 2, 4, and 6 correspond to saddle points, 5 is the Dirac point, and 3 and 7 are maximum intensity points. The corresponding fitted intensities of some of these points are plotted as a function of temperature. The two magnon peaks exhibit a somewhat different temperature dependence, with the upper branch (e.g., points 6 and 7) displaying a steeper drop in temperature compared to the lower branch (e.g., points 3 and 4). The acousticlike magnons of the lower branch would have spin deviations in the same directions within each layer, while the opticlike magnons of the upper branch would have the spin deviations go in opposite directions. We speculate that the opticlike magnons are more susceptible to decoherence and renormalization than the

acousticlike magnons, which may explain the steeper intensity drop at the higher-energy peak features. Regardless, similar behavior has been observed in materials like CrCl_3 [36].

Among the exchange constants in CoTiO_3 shown in the inset of Fig. 5(d) and values in Table I, the nearest-neighbor J_1 exchange constant emerges as the most significant within the system, possessing an in-plane component of $J_1 = -6.36$ meV and an out-of-plane component of $J_1 = 1.97$ meV. This observation provides further evidence for the presence of weak interplane interactions in the honeycomb lattice.

The magnetic intensity in the higher-energy range, 15 to 35 meV, is shown in Fig. 6(a) for 5, 42, and 300 K. At 5 K, two distinct peaks are observed at 26.7 and 28.6 meV, in addition to a shoulder at ~ 24 meV and a very weak peak at ~ 18 meV. The two peaks at 26.7 and 28.6 meV shift to lower energies upon increasing the temperature, while the intensity under the weak peak grows significantly. The most prominent excitations are from the magnetic excitons, which follow the same temperature dependence as the magnons. Specifically, the intensity at these peaks drops upon warming through the magnetic transition, as seen in Fig. 6(b). The intensity seen above T_N is most likely a spillover from the crystal field modes. On the other hand, the intensity at 18.5 and 23.9 meV exhibits the opposite temperature dependence [Fig. 6(b)], namely, the intensity grows through T_N and levels off by approximately 100 K before it gradually comes down but does not disappear. The intensity in that region, as seen in Fig. 6(a), becomes quite broad. The peak intensity around 18 meV most likely arises from crystal-field-split levels due to spin-orbit coupling [i.e., the D transition as labeled in Fig. 1(c)]. These modes grow in intensity with temperature as the corresponding energy levels become more thermally populated. A similar temperature dependence is observed in the data at ~ 58 meV [Fig. 4(b)], which most likely corresponds to the E transition in Fig. 1(c).

Co^{2+} bears a strong resemblance to Ir^{4+} and Ru^{3+} . In the iridates and ruthenates where only t_{2g} spins are present, Kitaev along with isotropic Heisenberg interactions were predicted to be important [21,37]. On the other hand, in d^7 systems, the additional e_g spins dramatically change the balance between the Kitaev and Heisenberg interactions. In CoTiO_3 specifically, the Heisenberg term is dominant and highly anisotropic [19]. In conclusion, we observed the temperature dependence of magnons, crystal field spin-orbit levels, and SOEs, all arising from the complex interplay of crystal field splitting and strong spin-orbit coupling in CoTiO_3 . Moreover, this measurement confirms the gapless nature of the Dirac magnons in this system.

ACKNOWLEDGMENTS

The authors would like to acknowledge discussions with Arun Paramakanti. The work at the University of Virginia is supported by the Department of Energy, Grant No. DE-FG02-01ER45927. The Spallation Neutron Source is a DOE Office of Science User Facility operated by Oak Ridge National Laboratory.

- [1] K. S. Novoselov, A. K. Geim, S. V. Morozov, D. Jiang, M. I. Katsnelson, I. V. Grigorieva, S. V. Dubonos, and A. A. Firsov, Two-dimensional gas of massless Dirac fermions in graphene, *Nature (London)* **438**, 197 (2005).
- [2] Y. Zhang, Y.-W. Tan, H. L. Stormer, and P. Kim, Experimental observation of the quantum Hall effect and Berry's phase in graphene, *Nature (London)* **438**, 201 (2005).
- [3] M. Franz and Z. Tešanović, Algebraic Fermi liquid from phase fluctuations: "Topological" fermions, vortex "Berryons", and QED₃ theory of cuprate superconductors, *Phys. Rev. Lett.* **87**, 257003 (2001).
- [4] S. S. Pershoguba, S. Banerjee, J. C. Lashley, J. Park, H. Ågren, G. Aepli, and A. V. Balatsky, Dirac magnons in honeycomb ferromagnets, *Phys. Rev. X* **8**, 011010 (2018).
- [5] S. K. Kim, H. Ochoa, R. Zarzuela, and Y. Tserkovnyak, Realization of the Haldane-Kane-Mele model in a system of localized spins, *Phys. Rev. Lett.* **117**, 227201 (2016).
- [6] P. A. McClarty, Topological magnons: A review, *Annu. Rev. Condens. Matter Phys.* **13**, 171 (2022).
- [7] F. Xue, Y. Hou, Z. Wang, and R. Wu, Two-dimensional ferromagnetic van der Waals CrCl₃ monolayer with enhanced anisotropy and Curie temperature, *Phys. Rev. B* **100**, 224429 (2019).
- [8] M. Elliot, P. A. McClarty, D. Prabhakaran, R. D. Johnson, H. C. Walker, P. Manuel, and R. Coldea, Order-by-disorder from bond-dependent exchange and intensity signature of nodal quasiparticles in a honeycomb cobaltate, *Nat. Commun.* **12**, 3936 (2021).
- [9] I. Y. Hwang, K. H. Lee, J.-H. Chung, K. Ikeuchi, V. O. Garlea, H. Yamauchi, M. Akatsu, and S. i. Shamoto, Spin wave excitations in honeycomb antiferromagnet MnTiO₃, *J. Phys. Soc. Jpn.* **90**, 064708 (2021).
- [10] J. B. Goodenough and J. J. Stickler, Theory of the magnetic properties of the ilmenites MTiO₃, *Phys. Rev.* **164**, 768 (1967).
- [11] B. Yuan, I. Khait, G.-J. Shu, F. C. Chou, M. B. Stone, J. P. Clancy, A. Paramakanti, and Y.-J. Kim, Dirac magnons in a honeycomb lattice quantum XY magnet CoTiO₃, *Phys. Rev. X* **10**, 011062 (2020).
- [12] B. Pato-Doldan, L. C. Gómez-Aguirre, A. P. Hansen, J. Mira, S. Castro-García, M. Sánchez-Andújar, M. A. Señaris-Rodríguez, V. S. Zapf, and J. Singleton, Magnetic transitions and isotropic versus anisotropic magnetic behaviour of [CH₃NH₃][M(HCOO)₃] M = Mn₂₊, Co₂₊, Ni₂₊, Cu₂₊ metal-organic perovskites, *J. Mater. Chem. C* **4**, 11164 (2016).
- [13] T. M. Holden, W. J. L. Buyers, E. C. Svensson, R. A. Cowley, M. T. Hutchings, D. Hukin, and R. W. H. Stevenson, Excitations in KCoF₃-I. experimental, *J. Phys. C* **4**, 2127 (1971).
- [14] W. J. L. Buyers, T. M. Holden, E. C. Svensson, R. A. Cowley, and M. T. Hutchings, Excitations in KCoF₃. II. theoretical, *J. Phys. C* **4**, 2139 (1971).
- [15] P. M. Sarte, S. D. Wilson, J. P. Attfield, and C. Stock, Magnetic fluctuations and the spin-orbit interaction in Mott insulating CoO, *J. Phys.: Condens. Matter* **32**, 374011 (2020).
- [16] P. M. Sarte, M. Songvilay, E. Pachoud, R. A. Ewings, C. D. Frost, D. Prabhakaran, K. H. Hong, A. J. Browne, Z. Yamani, J. P. Attfield *et al.*, Spin-orbit excitons in CoO, *Phys. Rev. B* **100**, 075143 (2019).
- [17] H. Wu, High spin and low spin mixed state in LaSrCoO₄: An *ab initio* study, *Phys. Rev. B* **81**, 115127 (2010).
- [18] K. Tomiyasu, M. K. Crawford, D. T. Adroja, P. Manuel, A. Tominaga, S. Hara, H. Sato, T. Watanabe, S. I. Ikeda, J. W. Lynn, K. Iwasa, and K. Yamada, Molecular spin-orbit excitations in the $J_{\text{eff}} = \frac{1}{2}$ frustrated spinel GeCo₂O₄, *Phys. Rev. B* **84**, 054405 (2011).
- [19] H. Liu and G. Khaliullin, Pseudospin exchange interactions in d^7 cobalt compounds: Possible realization of the Kitaev model, *Phys. Rev. B* **97**, 014407 (2018).
- [20] B. Yuan, M. B. Stone, G.-J. Shu, F. C. Chou, X. Rao, J. P. Clancy, and Y.-J. Kim, Spin-orbit exciton in a honeycomb lattice magnet CoTiO₃: Revealing a link between magnetism in d - and f -electron systems, *Phys. Rev. B* **102**, 134404 (2020).
- [21] G. Jackeli and G. Khaliullin, Mott insulators in the strong spin-orbit coupling limit: From Heisenberg to a quantum compass and Kitaev models, *Phys. Rev. Lett.* **102**, 017205 (2009).
- [22] P. Laurell, G. Alvarez, and E. Dagotto, Spin dynamics of the generalized quantum spin compass chain, *Phys. Rev. B* **107**, 104414 (2023).
- [23] R. Coldea, D. A. Tennant, E. M. Wheeler, E. Wawrzynska, D. Prabhakaran, M. Telling, K. Habicht, P. Smeibidl, and K. Kiefer, Quantum criticality in an Ising chain: experimental evidence for emergent E₈ symmetry, *Science* **327**, 177 (2010).
- [24] H. D. Zhou, C. Xu, A. M. Hallas, H. J. Silverstein, C. R. Wiebe, I. Umegaki, J. Q. Yan, T. P. Murphy, J. H. Park, Y. Qiu, J. R. D. Copley, J. S. Gardner, and Y. Takano, Successive phase transitions and extended spin-excitation continuum in the $s = \frac{1}{2}$ triangular-lattice antiferromagnet Ba₃CoSb₂O₉, *Phys. Rev. Lett.* **109**, 267206 (2012).
- [25] R. Rawl, L. Ge, H. Agrawal, Y. Kamiya, C. R. D. Cruz, N. P. Butch, X. F. Sun, M. Lee, E. S. Choi, J. Oitmaa, C. D. Batista, M. Mourigal, H. D. Zhou, and J. Ma, Ba₈CoNb₆O₂₄: A spin- $\frac{1}{2}$ triangular-lattice Heisenberg antiferromagnet in the two-dimensional limit, *Phys. Rev. B* **95**, 060412(R) (2017).
- [26] K. A. Ross, J. M. Brown, R. J. Cava, J. W. Krizan, S. E. Nagler, J. A. Rodriguez-Rivera, and M. B. Stone, Single-ion properties of the $S_{\text{eff}} = \frac{1}{2}$ XY antiferromagnetic pyrochlores NaA'Co₂F₇ (A' = Ca²⁺, Sr²⁺), *Phys. Rev. B* **95**, 144414 (2017).
- [27] B. Hälgl and A. Furrer, Anisotropic exchange and spin dynamics in the type-I (-IA) antiferromagnets CeAs, CeSb, and USb: A neutron study, *Phys. Rev. B* **34**, 6258 (1986).
- [28] L. J. Sandilands, Y. Tian, A. A. Reijnders, H.-S. Kim, K. W. Plumb, Y.-J. Kim, H.-Y. Kee, and K. S. Burch, Spin-orbit excitations and electronic structure of the putative Kitaev magnet α -RuCl₃, *Phys. Rev. B* **93**, 075144 (2016).
- [29] M. S. Spencer, Y. Fu, A. P. Schlaus, D. Hwang, Y. Dai, M. D. Smith, D. R. Gamelin, and X.-Y. Zhu, Spin-orbit-coupled exciton-polariton condensates in lead halide perovskites, *Sci. Adv.* **7**, eabj7667 (2021).
- [30] E. A. Dikushina and I. L. Avvakumov, Influence of a spin-orbit exciton on the magnetic ordering in Sr₂IrO₄, in *Physics, Technologies and Innovations (PTI-2016): Proceedings of the III International Young Researchers' Conference*, AIP Conf. Proc. No. 1767 (AIP, Melville, NY, 2016), p. 020034.
- [31] S. Toth and B. Lake, Linear spin wave theory for single-Q incommensurate magnetic structures, *J. Phys.: Condens. Matter* **27**, 166002 (2015).
- [32] M. Hoffmann, K. Dey, J. Werner, R. Bag, J. Kaiser, H. Wadepohl, Y. Skourski, M. Abdel-Hafiez, S. Singh, and R. Klingeler, Magnetic phase diagram, magnetoelastic coupling,

- and Grüneisen scaling in CoTiO_3 , [Phys. Rev. B **104**, 014429 \(2021\)](#).
- [33] K. Dey, M. Hoffmann, and R. Klingeler, Magnetostriction and magnetostructural domains in CoTiO_3 , [arXiv:2109.11923](#).
- [34] K. Dey, S. Sauerland, B. Ouladdiaf, K. Beauvois, H. Wadepohl, and R. Klingeler, Magnetostructural coupling in ilmenite-type NiTiO_3 , [Phys. Rev. B **103**, 134438 \(2021\)](#).
- [35] R. K. Maurya, N. Singh, and R. Bindu, Temperature evolution of the crystal structure of MnTiO_3 , in *Solid State Physics: Proceedings of the 59th DAE Solid State Physics Symposium 2014*, AIP Conf. Proc. No. 1665 (AIP, Melville, NY, 2015), p. 140013.
- [36] J. A. Schneeloch, Y. Tao, Y. Cheng, L. Daemen, G. Xu, Q. Zhang, and D. Louca, Gapless Dirac magnons in CrCl_3 , [npj Quantum Mater. **7**, 66 \(2022\)](#).
- [37] J. G. Rau, E. K. Lee, and H. Kee, Spin-orbit physics giving rise to novel phases in correlated systems: Iridates and related materials, [Annu. Rev. Condens. Matter Phys. **7**, 195 \(2016\)](#).